Atlantic Geoscience
Journal of the Atlantic Geoscience Society

Microbial components and metamorphic grade of Miaolingian (Cambrian) black shales from the Burin Peninsula, Newfoundland, Canada

Éléments microbiens et intensité du métamorphisme des schistes noirs miaolingiens (cambriens) de la péninsule de Burin, Terre-Neuve, Canada

Blanca Martínez-Benítez, Andrea J. Mills et J. Javier Álvaro

Volume 61, 2025

URI : https://id.erudit.org/iderudit/1118606ar
DOI : https://doi.org/10.4138/atlgeo.2025.008

Aller au sommaire du numéro

Éditeur(s)

Atlantic Geoscience Society

ISSN

2564-2987 (numérique)

Découvrir la revue

Citer cet article

Martínez-Benítez, B., Mills, A. & Álvaro, J. (2025). Microbial components and metamorphic grade of Miaolingian (Cambrian) black shales from the Burin Peninsula, Newfoundland, Canada. *Atlantic Geoscience*, *61*, 207–223. https://doi.org/10.4138/atlgeo.2025.008

Résumé de l'article

L'analyse des restes microbiens et palynologiques dans les schistes cambriens est utile à des fins biostratigraphiques et paléoécologiques, mais elle peut également servir à distinguer les températures d'enfouissement et de métamorphisme dans les affleurements affectés par un métamorphisme de contact. La composition microbienne des schistes noirs du Miaolingien provenant de la Formation de Pleasant View (Groupe d'Inlet) dans la péninsule de Burin est formée d'associations cyanobactériennes monospécifiques de Bavlinella faveolata, un taxon cosmopolite qui a caractérisé les épisodes d'eutrophisation au cours du Néoprotérozoïque au Miaolingien. Les spécimens présentent des degrés divers de dégradation sous microscopie pour examen par transmission et sous microscopie électronique à balayage à canon à émission de champ. Les spectres Raman de la thermométrie des matières carbonées appliqués aux microfossiles à paroi organique et aux réseaux de matière organique amorphe ont signalé des températures métamorphiques moyennes de 300 à 343 °C, alors que la valeur normalisée de l'indice de cristallinité de 0,37 ± 0,04 correspond à une position légèrement au-dessous de la limite entre l'anchizone et l'épizone, établie à 300 oC. L'estimation la plus probable de la température maximale de contact métamorphique enregistrée dans les échantillons de schistes noirs du Miaolingien, prélevés à proximité des intrusions granitiques du Dévonien supérieur de St. Lawrence, se situe dans l'intervalle de 300 à 350 °C.

Microbial components and metamorphic grade of Miaolingian (Cambrian) black shales from the Burin Peninsula, Newfoundland, Canada†

Blanca Martínez-Benítez[1, 2, *], Andrea J. Mills[3], and J. Javier Álvaro[1]

1. Instituto de Geociencias (CSIC-UCM), Dr. Severo Ochoa 7, Madrid 28040, Spain
2. Facultad de Ciencias Geológicas (UCM), Departamento GEODESPAL, José Antonio Novais 12, Madri, 28040, Spain
3. Geological Survey of Newfoundland and Labrador, Department of Industry, Energy and Technology, Government of Newfoundland and Labrador, St. John's, Newfoundland and Labrador A1B 4J6, Canada
* Corresponding author <blanca.m@igeo.ucm-csic.es>

Date received: 27 January 2025 ¶ Date accepted: 8 April 2025

ABSTRACT

The analysis of microbial and palynological remains in Cambrian shales is useful for biostratigraphic and palaeoecological purposes, but in outcrops affected by contact metamorphism, it can also be used for discriminating burial and metamorphic temperatures. The microbial composition of the Miaolingian black shale from the Pleasant View Formation (Inlet Group) in the Burin Peninsula consists of monospecific cyanobacterial associations of *Bavlinella faveolata*, a cosmopolitan taxon that characterized eutrophication episodes in Neoproterozoic to Miaolingian times. The specimens show varying degrees of degradation under transmitted light microscopy and field emission gun scanning electron microscopy. Raman spectra of carbonaceous materials thermometry applied to both the organic-walled microfossils and meshworks of amorphous organic matter has reported average metamorphic temperatures of 300 to 343°C, whereas the standardized Crystallinity Index Standard value of 0.37 ± 0.04 corresponds to a position slightly below the anchizone–epizone boundary, established at 300°C. The most likely fit for the peak contact metamorphic temperature recorded in the Miaolingian black shale samples, collected close to the Upper Devonian St. Lawrence granitic intrusions, is within the 300–350°C interval.

RÉSUMÉ

L'analyse des restes microbiens et palynologiques dans les schistes cambriens est utile à des fins biostratigraphiques et paléoécologiques, mais elle peut également servir à distinguer les températures d'enfouissement et de métamorphisme dans les affleurements affectés par un métamorphisme de contact. La composition microbienne des schistes noirs du Miaolingien provenant de la Formation de Pleasant View (Groupe d'Inlet) dans la péninsule de Burin est formée d'associations cyanobactériennes monospécifiques de *Bavlinella faveolata*, un taxon cosmopolite qui a caractérisé les épisodes d'eutrophisation au cours du Néoprotérozoïque au Miaolingien. Les spécimens présentent des degrés divers de dégradation sous microscopie pour examen par transmission et sous microscopie électronique à balayage à canon à émission de champ. Les spectres Raman de la thermométrie des matières carbonées appliqués aux microfossiles à paroi organique et aux réseaux de matière organique amorphe ont signalé des températures métamorphiques moyennes de 300 à 343 °C, alors que la valeur normalisée de l'indice de cristallinité de 0,37 ± 0,04 correspond à une position légèrement au-dessous de la limite entre l'anchizone et l'épizone, établie à 300 °C. L'estimation la plus probable de la température maximale de contact métamorphique enregistrée dans les échantillons de schistes noirs du Miaolingien, prélevés à proximité des intrusions granitiques du Dévonien supérieur de St. Lawrence, se situe dans l'intervalle de 300 à 350 °C.

[*Traduit par la redaction*]

INTRODUCTION

Water eutrophication, the process by which a water body becomes overly enriched with nutrients, was a common phenomenon during the Phanerozoic (e.g., Martin 1996; Large *et al.* 2015). In the sedimentary record, these episodes of eutrophication are usually represented by kerogenous black shale with a high Total Organic Carbon (TOC) per-

†From: Atlantic Geoscience Special Series "In recognition of the geological career of Sandra M. Barr". Atlantic Geoscience, 61, pp. 207-223.

ATLANTIC GEOSCIENCE 61, 207–223 (2025) doi:10.4138/atlgeo.2025.008
ISSN:2564-2987.

centage (Kennedy *et al.* 2002; Sageman *et al.* 2003). Coeval organic-rich black shales are found worldwide in formations such as the Miaolingian–Lower Ordovician Alum Shale of Scandinavia, which originated from algal-derived liptinite macerals (Nielsen and Schovsbo 2007; Hagenfeldt *et al.* 2023), the Miaolingian–Furongian Kistedalen Formation of Baltica (Palacios *et al.* 2022), the Miaolingian Manuels River Formation of the Avalon Peninsula of Newfoundland, and the Miaolingian Abbey Shale of southern England (Rushton 2011; Rees *et al.* 2014).

Marine transgressions (Botting *et al.* 2018) and volcanic episodes (Longman *et al.* 2021) are both known to increase nutrient flow to the oceans. The ash from nearby eruptions carries nutrients such as phosphorus and iron (Wu *et al.* 2023), whereas hydrothermal fluids linked to volcanism and tectonic activity can supply iron and rare earth elements (Frei *et al.* 2013). This sudden input of nutrients fertilizes the surface waters, triggering planktonic blooms that are well-documented in modern day coastal areas (Kelly *et al.* 2023; Schils 2012) and in the fossil record (Wu *et al.* 2023; Longman *et al.* 2021; Gaucher 2000; Gaucher *et al.* 2004; Zhang *et al.* 2024). A high degree of primary productivity on the upper water column generates a significant amount of organic matter that accumulates on the seafloor. The decomposition of that organic matter subsequently consumes the available dissolved oxygen, inducing bottom water anoxia (Canfield and Thamdrup 2009) and possibly euxinic conditions (Frei *et al.* 2013).

In western Avalonia, the beginning of Miaolingian times was characterized by a generalized transgression and flooding of an inherited horst-and-graben basin (Álvaro 2021; Mills and Álvaro 2023; Álvaro and Mills 2024) that recorded significant episodes of volcanic activity (e.g., Hay Cove volcanic rocks of Fletcher 2006; Chapel Arm Member of McCartney 1967; Mills and Álvaro 2023). The acritarch content of some Avalonian black shales (e.g., Flagg Cove, McNeil, and Manuel Rivers formations) has been locally studied in detail for biostratigraphic purposes (Hutchinson 1962; Martin and Dean 1981; Palacios *et al.* 2011; Johnson *et al.* 2024), but their kerogenous content had not yet attracted attention (but see discussions in Hutchinson 1962; Douglas 1983). An in-depth study of the black shales of the Manuels River Formation at its type locality (Conception Bay South, Newfoundland, Canada) reported a TOC percentage of up to 3.36% and a burial temperature of ca. 280°C, based on illite crystallinity (Austermann *et al.* 2021).

The study of the organic matter preserved in the Miaolingian black shales of western Avalonia is complicated, in the vicinity of Upper Devonian granites, by contact metamorphism. In the Little Lawn Harbour area of the Burin Peninsula, the black shales of the Pleasant View Formation are partly silicified and contain dispersed, black carbonaceous residue. The intrusion of the Upper Devonian St. Lawrence granite (Kerr *et al.* 1993; Magyarosi *et al.* 2019) has enhanced the thermal maturity of the organic matter and overprinted the geochemical signals related to eutrophication processes.

The aims of this paper are threefold: (i) to characterize the carbonaceous content preserved in the black shales of the Miaolingian Pleasant View Formation in Little Lawn Harbour; (ii) to test the effectiveness of the Raman Spectroscopy of Carbonaceous Materials (RSCM) thermometer on isolated organic-walled microfossil specimens extracted via acid maceration, and to compare the temperature results to those obtained via X-ray diffraction (XRD) and illite crystallinity; and (iii) to gain insight into the thermal evolution and metamorphic grade of sedimentary strata neighbouring Upper Devonian granites in the Burin Peninsula.

GEOLOGICAL CONTEXT

The Burin Peninsula is part of the Avalon Zone of Newfoundland (Fig. 1-inset), a part of the microcontinent of Avalonia, which likely originated as a volcanic arc off the west coast of Gondwana (O'Brien *et al.* 1996; Álvaro 2021 and references therein) recording some peri-Baltic influences (Beranek *et al.* 2023). This arc transitioned into a rift system (Nance *et al.* 2002) during latest Ediacaran to Miaolingian times (Álvaro 2021) and subsequently evolved into a passive margin across the Furongian and Ordovician (Nance *et al.* 2008; Satkoski *et al.* 2010). The evolution of Avalonia involved the formation of a Neoproterozoic volcano-sedimentary complex that constitutes the basement to the unconformably overlying marine sediment cover, deposited between the latest Ediacaran and the Ordovician (O'Brien at al. 1990, 1996; van Staal *et al.* 2020).

The Burin Peninsula has been the subject of several mapping campaigns during the 20th century, including those of Van Alstine (1948), Strong *et al.* (1976, 1978), and O'Brien *et al.* (1977). Cambrian shelly fossils were studied by Bengtson and Fletcher (1983) and Landing and Westrop (1998), and ichnofossils by Crimes and Anderson (1985) and Narbonne *et al.* (1987), which led to the definition of the Global Boundary Stratotype Section and Point of the Ediacaran–Cambrian boundary at Fortune Head (Narbonne *et al.* 1987). Recently, the uppermost Ediacaran–Cambrian cover sequence of the Avalon Zone has been studied by Fletcher (2006), structural analyses were conducted by Mills and Jones (2024), and Álvaro (2021) and Álvaro and Mills (2024) have conducted detailed analyses of carbonate production and penecontemporaneous hydrothermal activity. No detailed metamorphic study of the Cambrian rocks on the Burin Peninsula has yet been published. Hutchinson (1962) argued that the Cambrian cover sequence on the Burin Peninsula displays a lower metamorphic grade than it does on the Avalon Peninsula. Regarding the latter, Papezik (1974) argued for an east-west gradient from prehnite–pumpellyite to greenschist facies. However, more recent work by Austermann *et al.* (2021) supports a gradient from greenschists facies at Bonavista to low-grade metamorphism and late diagenesis westwards. Mills and Jones (2024) reported evidence of contact metamorphism in areas proximal to the Upper Devonian St. Lawrence granitic intrusion.

The South Burin area (Fig.1) is divided into three struc-

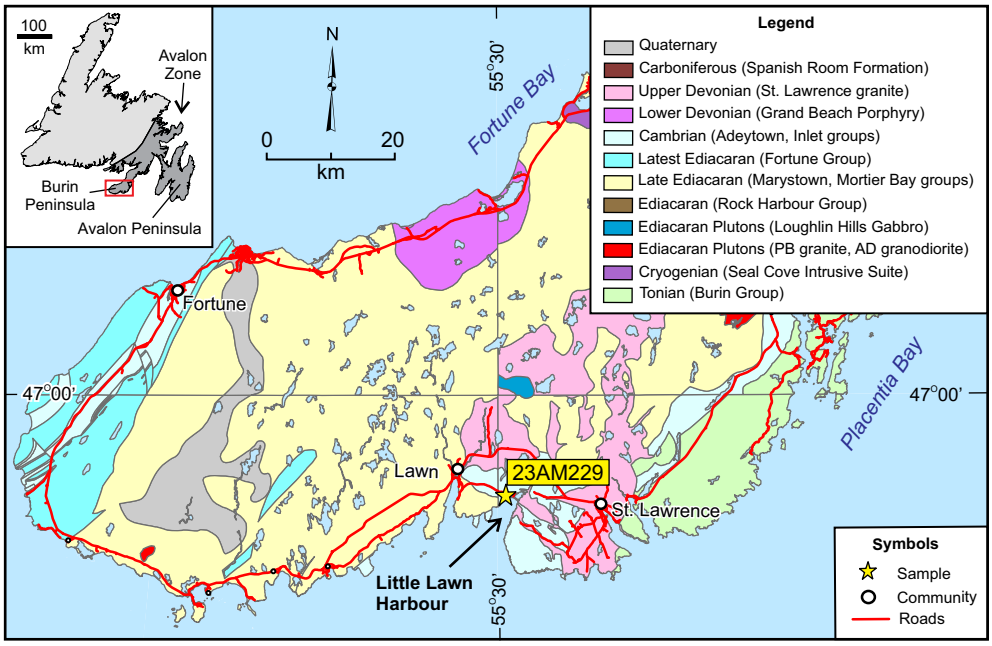

Figure 1. Simplified geological map of the Burin Peninsula, Newfoundland, modified after Strong *et al.* (1978) and Mills and Jones (2024), showing the location of sample 23AM229. Inset map shows the location of the geological map (red box) and the Burin and Avalon peninsulas in the Avalon Zone of Newfoundland.

tural units (Strong *et al.* 1978), known as the West, Central and East domains. The main stratigraphic units of the central domain are the Ediacaran volcano-sedimentary Marystown Group, the Cambrian Inlet Group and the Upper Devonian St. Lawrence Granite (Mills and Jones 2024). The Inlet Group (Strong *et al.* 1978) is composed of marine sedimentary rocks unconformably overlying the volcano-sedimentary Burin (Strong *et al.* 1978) and Marystown (Sparkes and Dunning 2014) groups. It comprises three formations, from base to top, the Bay View, Salt Pond and Pleasant View formations (Strong *et al.* 1978) (Fig. 2). The Miaolingian Pleasant View Formation, the focus of this research, has a lower member of grey limestone and dark grey siltstone that grades upwards into a light green and red mudstone, and an upper member of black, highly fissile shale, and dark grey siltstone with light grey limestone nodules (Strong *et al.* 1978). Both members are rich in trilobites, reported by Van Alstine (1948) and Strong *et al.* (1978). The presence of trilobites from the *Paradoxides davidis* and *Hydrocephalus hicksii* zones in the black shales of the upper member provides a Miaolingian age for the unit and allows biostratigraphic correlation with the Manuels River Formation of the Avalon Peninsula (Strong *et al.* 1978).

The samples studied here were collected from outcrop in Little Lawn Harbour (46.92896°N/–55.481881°W), located between the towns of Lawn, to the west, and St. Lawrence, to the east. In this outcrop, the Pleasant View Formation consists of black and dark grey-green shale, with pyrite veinlets up to 5 mm thick (Fig. 3). These shales are partly silicified, fracture conchoidally, and show tightly spaced and highly penetrative cleavage (Mills and Jones 2024).

MATERIAL AND METHODS

Organic matter preserved in marine strata commonly records a series of extensive biogeochemical transformations as a consequence of burial (Beyssac *et al.* 2002) and, in this case study, by contact metamorphism (Mills and Jones 2024). As these transformations progress, both amorphous and "poorly organized" organic matter, which have a significant degree of disorder in their internal structure, gradually acquire the well-ordered and crystalline structure of graphite (Pasteris and Wopenka 2003). This biogeochemical transformation can be tracked using different techniques: change in colour of the organic matter from clear yellow to black, as semi-quantified by the Thermal Alteration Index (TAI) (Hayes *et al.* 1983), X-ray diffraction (Landis 1971) and Raman spectrometry (Beyssac *et al.* 2002).

Sample 23AM229 is a greyish-black, laminated shale with high pyrite content. To extract the organic walled microfossils, the sample was subjected to acid digestion following the palynological technique first developed by Vidal (1988) and later adjusted by Palacios *et al.* (2022) in the Department of Palaeontology at the University of Extremadura (UNEX), Badajoz, Spain. The sample was shattered into small fragments and macerated in 40% concentration hydrofluoric acid for a period of two weeks. Two subsequent chemical treatments were applied, each followed by a filtering process: boiling in hydrochloric acid to remove the fluorides creat-ed during the maceration, and the addition of hot HNO_3 to eliminate most of the pyrite. The resulting liquids were filtered using a 20 µm SEFAR mesh membrane, obtaining a concentrated organic residue that was preserved for long-term storage in ethanol.

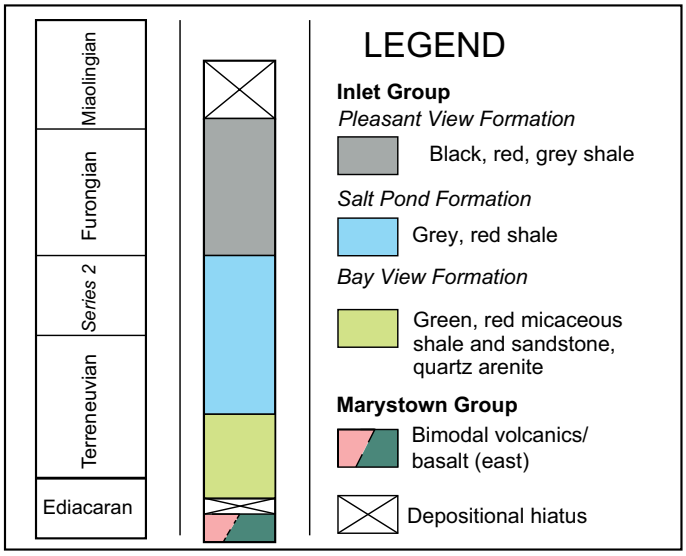

Figure 2. Simplified stratigraphic column of the Burin Peninsula, Newfoundland, showing the Inlet Group, modified from Strong *et al.* (1978) and Mills and Jones (2024).

Figure 3. Field photograph of the Pleasant View Formation black shale sampled for this study. Yellow arrow points to pyrite vein; pocketknife for scale is 9 cm long.

Transmitted light microscopy and Field Emission Gun Scanning Electron Microscopy (FEGSEM)

Palynological slides were made using the organic residue alongside a Petropoxy 154 resin (Burnham Petrographics LLC). They were studied with a ZEISS Axio Imager Microscope equipped with an Axiocam HRc digital camera at UNEX. Photographs taken at different heights were composited using CombineZP software. For FEGSEM analysis, several drops of insoluble residue were deposited onto a bio-adhesive strip, and the alcohol was left to evaporate. The photomicrographs were taken using an Apreo 2S Termofisher Cryo-FEGSEM housed at the Non-Destructive Technique Service (STND) at the National Museum of Natural Sciences (MNCN) in Madrid, employing the secondary electrons (SE) mode, with the Everhart-Thornley detector and at 5 kV of voltage. Some of the photomicrographs were taken using the CRYO mode of FEGSEM, in which the sample is flash-frozen using liquid nitrogen before photography. The specimens' measurements were taken using ImageJ (Abrámoff *et al.* 2004) software.

Confocal Raman Spectroscopy and RSCM thermometer

Raman spectrometry has been employed extensively to measure the degree of amorphous organic matter (AOM) maturity, as it allows for rapid, non-destructive sampling of different parameters simultaneously (Henry *et al.* 2019). The Raman spectra of organic matter is characterized by the presence of two main bands in the first order region (Tuinstra and Koenig 1970): (i) the graphite band or G-band is located at ca. 1600 cm^{-1} (Henry *et al.* 2019) and is the result of in-plane vibration of aromatic carbons in the graphite structure (Beyssac *et al.* 2002); and (ii) the disorder band, or D-band, is found at ca. 1350 cm^{-1}, and is the product of in-plane defects caused by the presence of heteroatoms in the crystal structure (Beny-Bassez and Rouzaud 1985). The properties of both bands, such as peak position, intensity ratio, or full width at half measure (FWHM), change according to modifications in the degree of crystallinity and the thermal evolution of the sample (Pasteris and Wopenka 2003), but can also be affected by the original complexity of the organic matter precursor (Bower *et al.* 2013).

Raman spectrometry has been successfully used to measure the thermal maturity of acritarchs dating as far back as the Mesoproterozoic and Neoproterozoic (Marshall *et al.* 2005; Arouri *et al.* 2000; Álvaro *et al.* 2024). The Raman Spectroscopy of Carbonaceous Materials (RSCM) thermometer was first developed by Beyssac *et al.* (2002) for metasedimentary rocks in the 330–650°C temperature range. Lahfid *et al.* (2010) expanded that temperature range to 200°C, into low-grade metamorphic conditions. In their methodological review, Henry *et al.* (2019) summarized the suitable analytical practices of this technique and associated challenges.

The analyses were performed using the Thermofisher XRD Raman Confocal Microscope, with attached Atlus camera at the STND of the MNCN. The spectrometer is equipped with an aperture of 25 μm, a 400 mm/lines grating and a spot size of 3.1 μm. The sampling parameters are adapted from the methodology of Henry *et al.* (2019), modified to consider that the Raman laser available at the MNCN has a slightly weaker 532 nm wavelength. Laser potency was 0.4 MW, with a sample exposure time of 20 s, 4 sample exposures and the 50x objective. For analysis of the standard parameters of the spectra, such as peak positions, the intensity ratio and the FWHM of the main band peaks, software Spectragryph (Menges 2022) was used. The digital treatment of the spectra was done applying the software OMNIC (Thermofisher), and the spectra deconvolution was achieved with the Peak Resolve tool.

Prior to Raman analysis, the organic residue was washed

free of alcohol, avoiding interferences with the Raman signal of the AOM and facilitating disaggregation. To that end, a small quantity of the residue was extracted using a Pasteur pipette and deposited in a new vial, where it was left to set. Distilled water was added to the vial and left in repose until all the AOM sunk to the bottom. Then, the extra water was removed, and the vial was filled again. This procedure was repeated three times. Once the sample was free of alcohol, a few drops were deposited in a strew section. The sample points chosen all correspond to identifiable specimens. Following Henry *et al.* (2019), intra-particle variability was reduced, with 3–5 spectra taken at each sample point, and thin parts and edges of the specimen were avoided. The selected spectral range, from 2000 to 900 cm^{-1}, covers the first order region of the AOM spectra (Tuinstra and Koening 1970).

The three best spectra of each targeted point were selected based on their signal-to-noise ratio and their intensity and averaged to reduce intraparticle heterogeneity. This averaged spectrum was then subjected to smoothing using the Savitzky-Golay smoothing filter with a 21-point quadratic polynomial algorithm (Savitzky and Golay 1964). Finally, spectra deconvolution was undertaken following the five-band criteria of Lahfid *et al.* (2010), and a Voigt profile for the bands (Beyssac *et al.* 2002). To calculate palaeotemperatures, the area ratios and linear equations of Beyssac *et al.* (2002: R2), and Lahfid *et al.* (2010: RA1 and RA2) were used. These three parameters were employed simultaneously because, based on previous indicators (Hayes *et al.* 1983; Bower *et al.* 2013) (TAI, shape of the spectra), sample 23AM229 is believed to be located near the RA1/RA2 upper boundary, and the R2 lower boundary. As such, using all three ratios will offer a more accurate range, and reduce the error associated with results that are close to the limits of each parameter.

$$R2 = D1/(G+D1+D2)$$

$$RA1 = (D1+D4)/(D1+D2+D3+D4+G)$$

$$RA2 = (D1+D2)/(D2+D3+G)$$

$$TR2(°C) = -445R2+641$$

$$TRA1(°C) = (RA1-0.3758)/0.0008$$

$$TRA2(°C) = (RA2-0.27)/0.0045$$

XRD, Kübler Index, and "Crystallinity Index Standard" (CIS) for illite

The Little Lawn Harbour samples were washed, coarsely crushed, and homogeneous chips were selected for X-ray diffraction (XRD) analysis. For whole-rock and clay fraction analysis, the samples were milled in an agate mortar and prepared as disoriented powders and oriented aggregates. The <2 μm clay fraction was extracted by repeated centrifugation and supernatant removal, following Stokes's law. Oriented aggregates were obtained by sedimentation on glass slides.

XRD analysis was conducted using a PANalytical X'Pert Pro diffractometer (Malvern Panalytical, Malvern, UK) with CuKα radiation (45 kV, 40 mA) and an X'Celerator solid-state linear detector at the XRD laboratory of the Mineralogy and Petrology Department at the University of Granada (Spain). The measurements were taken with a step increment of 0.008° 2θ and a total counting time of 10 s/step. Bulk rock and oriented clay analyses were also undertaken using the STND's non-destructive D8 Discover A25 Bruker microdifractometer, equipped with a CuKα source and a diffraction angle 2θ ranging from 2–70°. To prepare the oriented samples at the STND, the powdered sample was mixed with distilled water, left to decant, and the clay fraction then removed again, divided into three sub-samples, each subjected to a different treatment: (i) air dried at room temperature; (ii) saturated in ethylene-glycol and left to air dry at room temperature; (iii) heated to 550°C for a period of three hours.

For illite "crystallinity" determination, sample preparation and Kübler Index (KI) measurements followed the experimental conditions recommended by the IGCP 294 IC Working Group (Kisch 1991). KI values (x) were converted into CIS values (y) using the equation $y = 0.972x + 0.1096$ ($r = 0.970$), following the international standards of Warr and Rice (1994) and Warr (2018). As KI and CIS scales are not equivalent (Warr and Ferreiro-Mahlmann 2015), the anchizone limits for CIS are set between 0.32 and 0.52° Δ2θ.

The measurement of the TOC content of the sample was performed at MNCN using an elemental analyser Perkin Elmer 2400 Series II, which measures both the total carbon and the inorganic carbon content, thereby obtaining TOC by subtraction of those values.

RESULTS

Macerated residue

The study of the organic residue using the transmitted light microscope, the Confocal Raman spectrometer and the FEGSEM has shown that its principal component consists of monospecific associations of *Bavlinella faveolata* (Fig. 4a–g), encased in meshworks of amorphous organic matter (Fig. 4d, f). Clusters of <5 μm long needle-like crystals (Fig. 4d), have been identified as rutile accumulations based on their Raman spectra. The AOM shows a significant degree of thermal alteration, with a black colour indicating a TAI = 5 (Hayes *et al.* 1983). In FEGSEM, the AOM is revealed to be composed, to a significant degree, by partly degraded debris of *Bavlinella faveolata* (Fig.4e, g).

Raman parameters and RSCM

The Raman spectra of both AOM remains and individualized specimens share the same arrangement, with two narrow bands separated by a saddle, with the D1-band located at ca. 1344.52 ± 1.25 cm^{-1} and the G-band at ca. 1596.84 ± 1.24 cm^{-1} (Fig. 5a). The D1-band is the strongest, leading to

R1 ratio of 1.17 ± 0.02, and wider, with a FWHM of 74.62 ± 2.62 cm^{-1}, in contrast to the G-band's at 53.74 ± 2.79 cm^{-1}. The saddle is only visible in the spectra that record the highest intensities, probably due to the low voltage employed. After deconvolution (Fig. 5b), the position of D4 (1279.13 ± 2.79 cm^{-1}) and D3 (1547.49 ± 3.98 cm^{-1}) bands shifts towards higher positions. D2 occurs in the expected position at 1618.75 ± 0.72 cm^{-1} (Table 1).

The average area ratio values obtained are: R2 = 0.67 ± 0.03, RA1 = 0.65 ± 0.01 and RA2 = 1.65 ± 0.09, which correspond to mean temperatures of T(R2) = 343.71 ± 12.38°C, T(RA1) = 339.36 ± 16.45°C, and T(RA2) = 305.81 ± 20.85°C. The lowest temperature recorded is 271.97 ± 20.85°C at sample point 7, and the highest is 365.70 ± 16.45°C at sample point 8 (Table 2).

XRD and illite crystallinity

The bulk rock diffractogram from the STND indicates that the sample powder is composed of quartz, illite, chamosite, pyrite and albite (Fig. 6a). There is no visible shift in peak position between the air-dried sub-sample and the ethylene-glycol saturated subsample (Fig. 6b). The CIS values obtained using the equation referenced in the method section oscillate between 0.33–0.42, with an average of 0.37 ± 0.04.-

Total organic carbon (TOC)

The Bernard calcimeter reports that the total percentage of carbon in the sample is 0.35%, of which 0.15% is carbonate and 0.20 % is TOC.

SYSTEMATIC PALAEONTOLOGY

Phylum **Cyanobacteria** Stanier *et al.* 1978

Genus ***Bavlinella*** (Schepeleva) Vidal 1976

Type species. *Bavlinella faveolata* Shepeleva 1962, emended Vidal 1976

Bavlinella faveolata Shepeleva 1962, emended Vidal 1976
Fig. 4a–c, f–h_1

Remarks. *Bavlinella faveolata* was first defined as *Bavlinella faveolatus* by Shepeleva (1962). Subsequently, Moorman (1974) described the species *Sphaerocongregus variabilis*, which Vidal (1976) interpreted as a junior synonym of *Bavlinella faveolata*. However, Muir (1977) and Foster *et al.* (1985), among others, argued that the specimen from Visingsö (Sweden) illustrated by Vidal (1976) was a framboidal pyrite. In subsequent articles the name *Sphaerocongregus variabilis* was used (Mansuy and Vidal 1983; Vidal and Nystuen 1990). Nevertheless, German *et al.* (1989) had already designated a lectotype for *Bavlinella faveolata* based on material from the Kotlin Formation (Gaucher *et al.* 2003), further illustrated by Schopf (1992). Therefore, due to the official designation of a lectotype, *Sphaerocongregus variabilis* Moorman (1974) should be considered a junior synonym of *Bavlinella faveolata* (Gaucher *et al.* 2003).

Material. Hundreds of specimens were prepared in palynological slides and FEGSEM preparations, made with the residue obtained after palynological maceration of partly silicified black shales extremely rich in authigenic and framboidal pyrite. The specimens show varying degrees of physical degradation and a high degree of thermal alteration.

Description. In thin-section (2D), each specimen is sub-rounded, with a surface composed of small subspherical cells, only visible in rare semi-transparent individuals (Fig. 4a), the vast majority being too opaque to see through (Fig. 4b). In the Darkfield mode of the Confocal Raman spectrometer, it is possible to observe the surface of opaque specimens, although not in great detail (Fig. 4c). The FEGSEM photomicrographs yield distinct views of 3D morphologies. Isolated specimens are rare, the majority appearing in aggregates of 2–3 spheres (Fig. 4f). In the best-preserved specimens, it is possible to distinguish a thin outer vesicle layer, covering a hexagonal honeycomb pattern emphasizing its positive relief (Fig. 4g, h_1). The cells in the pattern are hollow, separated by thin walls and, in most specimens, damaged and deformed to different degrees (Fig. 4f, g). Smaller

Figure 4. (next page) (a) Photomicrograph of a semi-transparent specimen of *Bavlinella faveolata* in thin section. (b). Photomicrograph of an opaque specimen of *Bavlinella favelota* in thin section. (c) Photomicrograph of an opaque specimen of *Bavlinella faveolata* as seen in darkfield mode in the Confocal Raman Microscope. Once darkfield mode is active, the interior morphology seen in the semi-transparent specimens becomes visible. (d) Photomicrograph of a cluster of amorphous organic matter (AOM), in which some specimens of *Bavlinella faveolata* are visible. The red arrows point to rutile crystals. (e) FEGSEM photomicrograph of AOM showing that its main components are degraded fragments of *Bavlinella faveolata.* (f) CRYO-FEGSEM photomicrograph showing a degraded association of at least four vesicles of *Bavlinella faveolata*. The hollow interior of the vesicles is visible. (g) CRYO-FEGSEM photomicrograph showing a meshwork of AOM composed of degraded specimens of *Bavlinella faveolata* (left), and an individual vesicle that preserves part of the outer layer (right). In the lower half of the vesicle, the outer layer has been destroyed, leaving the hexagonal cells visible. (h) FEGSEM photomicrograph of several specimens of *Bavlinella faveolata* alongside rutile crystals (red arrows). The specimens differ in size and in the density of a honeycomb pattern. (h_1) Close up of (h), in which the outer vesicle layer is visible, covering most of the hexagonal cells. Scale bars: a, b = 5 μm; c–e, h = 10 μm; f, g, h_1 = 4 μm.

specimens have a denser distribution of smaller cells that are not as distinctly hexagonal in shape as those found in larger individuals (Fig. 4g).

Dimensions. In thin-section, specimens range in diameter from 3.1 to 9.1 μm (mean = 5.73 μm, σ = 1.58 μm, N = 31), and the cells are too small to be measured with the ZEISS microscope. In FEGSEM, the size of individual specimens ranges from an outlier of 3.27 to 12.39 μm (mean = 5.94 μm, σ = 2.85, N = 10). Cell sizes range from 0.30 to 1.15 μm (mean = 0.54, σ = 0.25, N = 18). It is remarkable that even the best-preserved specimens display deformed and

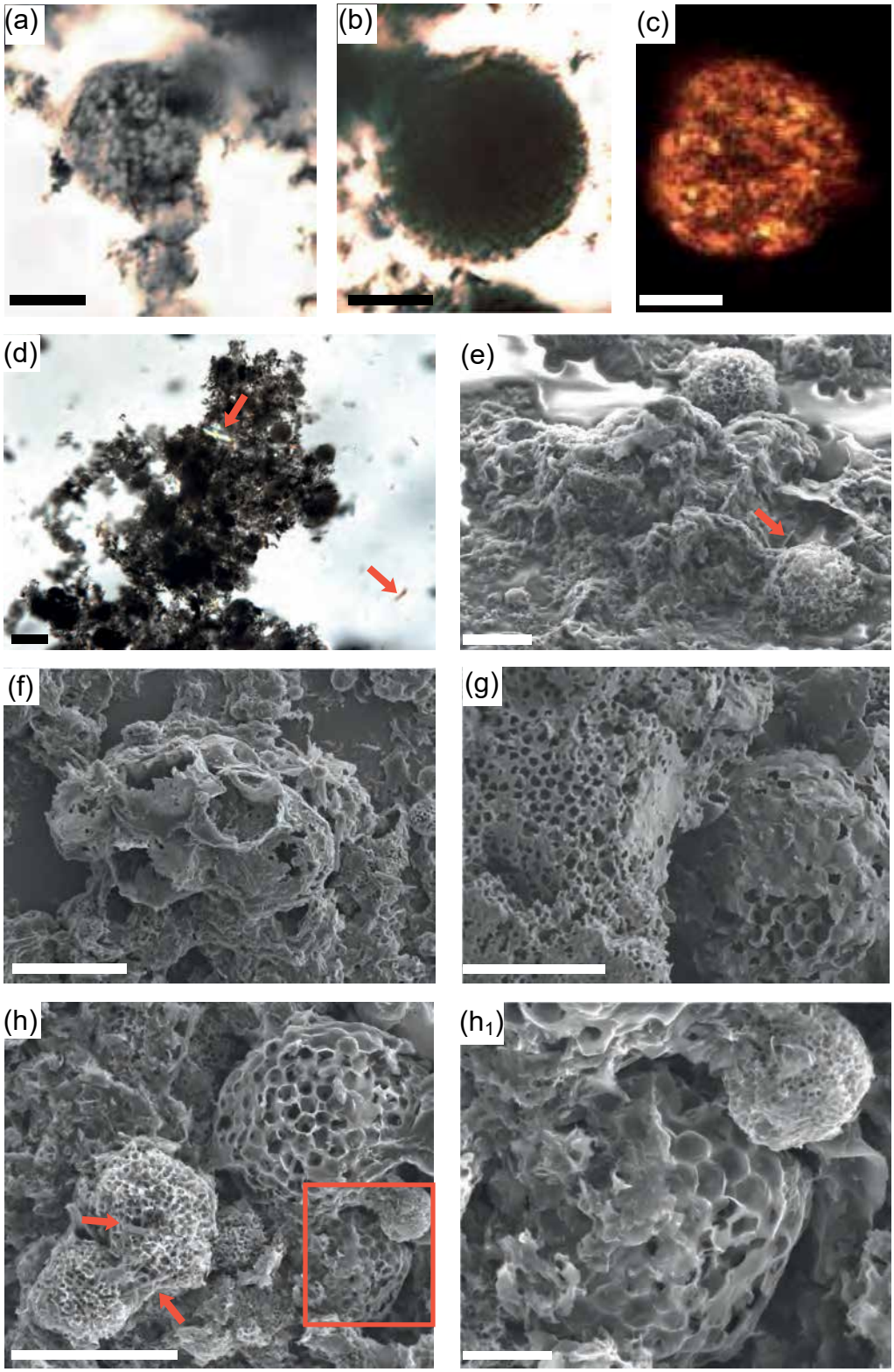

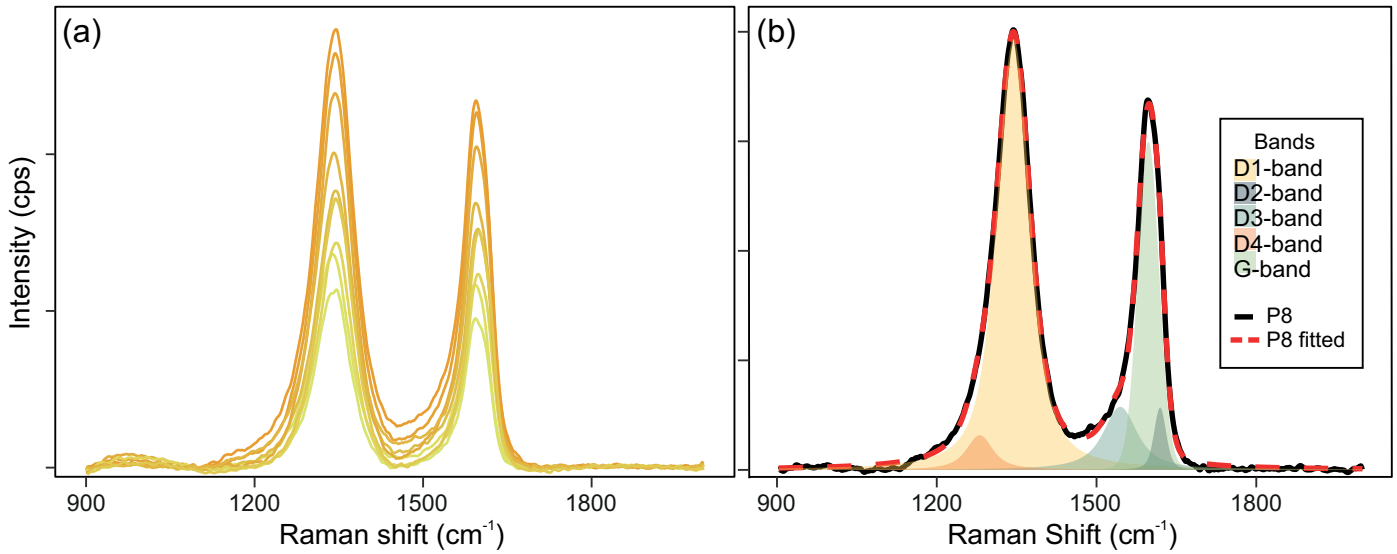

Figure 5. (a) Overlapping Raman spectra of nine sampled points, after averaging and smoothing. (b) Deconvolution of the Raman spectrum corresponding to sampling point 8, with the five bands in colour. Black line indicates the averaged and smoothed spectrum prior to deconvolution, the red dashed line the fitted spectrum obtained with Peak Resolve.

damaged cells, somewhat controlling the final size and shape of the specimens.

Comments. *Bavlinella faveolata* is a cosmopolitan fossil, with a chronological range from the Cryogenian to the Ordovician (Gaucher and Sprechman 1999; Reitz 1991) and possibly reaching the Carboniferous (Shkrebta *et al.* 1973). It has been reported from the Iberian Peninsula (Palacios 1983; Álvaro *et al.* 2024), the Volga-Ural province (Shepeleva 1962), the East European Platform (German *et al.* 1989; Schopf 1992), South Africa (Gaucher and Germs 2006), Namibia (Gaucher *et al.* 2005), Germany (Pflug and Reitz 1992), Uruguay (Gaucher 2000; Frei *et al.* 2013), Brazil (Chiglino *et al.* 2015), and Norway (Palacios *et al.* 2022). In Norway (Vidal and Nystuen 1990), South Australia (Foster *et al.* 1985), Arizona, USA (Nagy *et al.* 2009), and Alberta, Canada (Moorman 1974), some specimens have also been reported as *Sphaerocongregus variabilis*.

Although *Bavlinella faveolata* is abundant after acid maceration of black shales (Palacios *et al.* 2022), it has also been reported from thin-sections of chert (Frei *et al.* 2013) and black limestone (Chiglino *et al.* 2015), and as etching residue of phyllitic mica schists (Pflug and Reitz 1992), kerogenous marlstones and limestones (Gaucher *et al.* 2005; Gaucher and Germs 2006), and greywackes and siltstones (Gaucher *et al.* 2003; Álvaro *et al.* 2024). Variably preserved

Table 1. Band position and FWHM.

Sample Point	D1 position	D2 position	D3 position	D4 position	G position	D1 FWHM	G FWHM
P1	1344.9	1618.81	1547.26	1277.91	1598.1	75.32	53.591
P2	1343.6	1618.78	1544.24	1281.76	1595.2	76.357	55.406
P3	1347.1	1620.02	1550.95	1274.83	1595.8	70.983	51.968
P4	1344.3	1618.71	1544.61	1280.85	1597.4	76.109	54.539
P5	1343.2	1617.68	1546.16	1280.55	1595	73.354	54.359
P6	1345	1617.75	1545.01	1276.95	1597.4	76.109	54.539
P7	1345.4	1618.79	1548.31	1282.82	1598	71.834	52.543
P8	1344	1619.39	1544.51	1280.54	1596.6	79.075	54.992
P9	1343.2	1618.85	1556.34	1275.98	1598.1	72.477	51.764
Average	1344.52	1618.75	1547.49	1279.13	1596.84	74.62	53.74
σ (±)	1.25	0.72	3.98	2.79	1.24	2.62	1.35

Table 2. RSCM results and corresponding temperatures.

Sample Point	R1	R2	RA1	RA2	T = °C (R2)	T = °C (RA1)	T = °C (RA2)
P1	1.17	0.67	0.66	1.74	340.81	358.03	327.74
P2	1.17	0.68	0.64	1.62	338.85	330.09	299.97
P3	1.21	0.65	0.65	1.65	351.13	346.47	307.39
P4	1.16	0.66	0.65	1.62	346.44	337.64	300.06
P5	1.17	0.66	0.63	1.60	346.23	318.66	295.47
P6	1.19	0.72	0.66	1.74	322.57	349.58	325.78
P7	1.16	0.62	0.63	1.49	365.24	322.62	271.97
P8	1.19	0.7	0.67	1.78	331.04	365.7	336.48
P9	1.14	0.65	0.64	1.56	351.11	325.4	287.47
Average	1.17	0.67	0.65	1.65	343.71	339.36	305.81
σ (±)	0.02	0.03	0.01	0.09	12.38	16.54	20.85

microfossils in sedimentary rocks recording low-grade metamorphism have been reported by Foster *et al.* (1985) and Downie *et al.* (1971). Foster *et al.* (1985) argued that, because of their composition and small size, specimens of *Sphaerocongregus variabilis* (= *Bavlinella faveolata*) are resistant to tectonometamorphic effects.

Recovery of abundant remains of *Bavlinella faveolata* offers a unique opportunity for the application of the RSCM thermometer due to: (i) its long chronological range; (ii) its cosmopolitan character; (iii) its simple extraction via acid maceration, although time consuming, yielding many specimens and a high number of targeted points for analysis in strew section; and (iv) its uncomplicated taxonomic identification under both confocal Raman microscopy and FEGSEM microscopy, as its morphology is not deeply damaged by low grade metamorphism (Downie *et al.* 1971; Foster *et al.* 1985), preserving most of its volume and features intact up to the beginning of the greenschist facies (Stanevich *et al.* 2005).

DISCUSSION

Bavlinella faveolata has been interpreted as both microbial remains and dubiofossils. Originally, Shepeleva (1962) defined the species based on 2D thin-sections, but Vidal (1976) assigned to the species one specimen illustrated with 3D stereoscan photomicrographs, which was later identified as a framboidal pyrite (Muir 1977; Foster *et al.* 1985). Muir (1977) suggested subsequently that the genus *Bavlinella* Shepeleva 1962 may represent a junior synonym of *Pyritosphaera* Love, 1958, a framboidal pyrite mixed with intercrystalline amorphous organic matter (see also MacLean *et al.* 2008: fig. 2A). This confusion raised doubts about the taxonomic validity of the species. However, subsequent illustrations in 2D and 3D of *Bavlinella faveolata*, alongside analysis of its organic content, have been reported from Cryogenian to Carboniferous strata (Shkrebta *et al.* 1973; Chiglino *et al.* 2015; Gaucher *et al.* 2005, 2008; Prasad *et al.* 2010; Vavrdová 2008; Yin and Yuan 2007). Recently, Álvaro *et al.* (2024) supported a cyanobacterial affinity for specimens of *Bavlinella faveolata* in material extracted from the uppermost Ediacaran greywackes of the Cíjara Formation in Spain, based on: (i) Raman spectra of both the microfossils and their associated (partly degraded) AOM, and (ii) some characteristic biomarkers containing the alkanes 17:1 and 7-methyl-heptadecane together with the saturated fatty acids 16:0, the unsaturated fatty acids 18:1ω7, 16:1 ω7, 18:2 ω6 and 18:3 ω6, and hexose and pentoses, sugar moieties that are part of heterocyst glycolipids.

In general, *Bavlinella faveolata* is commonly found in rocks that originated in dysoxic to anoxic environments (Frei *et al.* 2013). Massive occurrences of *Bavlinella faveolata*-dominant (nearly monospecific) assemblages in Neoproterozoic strata have been interpreted as cyanobacterial blooms related to the eutrophication of vast oceans (Gaucher *et al.* 2008; Nagy *et al.* 2009; Álvaro *et al.* 2024). However, since Cambrian times, their occurrences are no longer monospecific, and specimens co-occur as subsidiary elements mixed with chronostratigraphically diagnostic acritarchs (Yin *et al.* 2018; Le Hérissé *et al.* 2017; Palacios *et al.* 2022).

The main taxonomic problem of this genus and species, commonly found as spherical aggregates, relates to their traditional 2D characterization, where part of their image is necessarily out of focus. Considering the lack of distinct diagnostic characters in 2D and the similar morphology currently exhibited by some cyanobacteria (such as *Microcystis* Kützing, 1833, a unicellular cyanobacterial genus bearing gas-filled vesicles and lacking individual sheaths and known to regulate its buoyancy and form dense blooms; Den Uyl *et al.* 2021), the morphotype of *Bavlinella faveolata* does not necessarily represent a single biological species but may represent a "wastebasket taxon" (Plotnick and Wagner 2006), a designation for specimens whose correct identification is essentially impossible ("taphonomic wastebasket") or

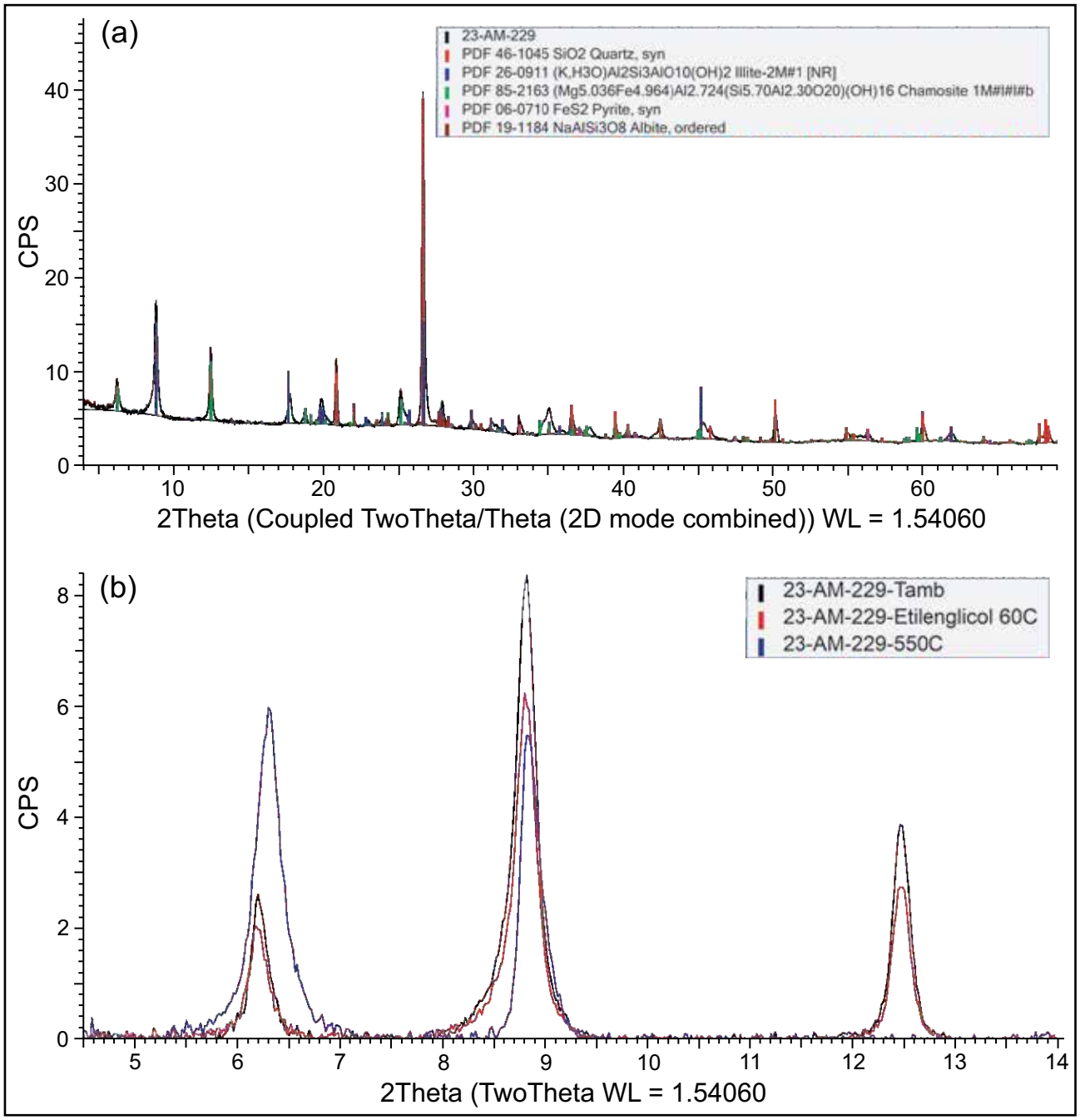

Figure 6. (a) X-ray diffraction (XRD) diffractogram of sample 23AM229, with peaks corresponding to the main components of the sample. (b) XRD of oriented clay aggregates after being left to dry at room temperature (black), hydrated with ethylene-glycol (red), and heated up to 550ºC for three hours (blue).

have been erroneously described and classified ("systemic wastebasket"). *Bavlinella faveolata*'s simple morphology in thin-section (circular disks with sub-spherical surfaces that are not commonly visible in transmitted light) has led to inappropriate assignations with other organic or inorganic components, such as framboidal pyrite (Muir 1977; Foster *et al.* 1985; MacLean *et al.* 2008). For a correct identification of this taxon, SEM microphotography is a fundamental step.

Recently, Palacios *et al.* (2022) reported that the vesicles of *Bavlinella faveolata* obtained from Miaolingian black shales of Norway are not degraded. Based on this observation, the authors suggested that the taxon may be a sulphur-reducing bacteria linked to the degradation of organic matter and pyrite formation. Because 2D illustrations lack the necessary resolution to determine the degree of degradation of individual vesicles, or to identify the AOM components, 3D images are necessary to solve this question. The degradation of the Pleasant View Formation specimens is visually distinct (Fig. 4e–g). Most vesicles have completely lost their outer layer, and their hexagonal honeycomb pattern is incomplete,

deformed and damaged (Fig. 4e–h). Degraded fragments of *Bavlinella faveolata* constitute also the main component of the AOM meshwork (Fig. 4f). Furthermore, monospecific organic remains have so far only yielded specific cyanobacterial biomarkers (Álvaro *et al.* 2024).

To determine peak metamorphic temperatures, several parameters are commonly used to constrain temperature ranges, such as the degree of thermal alteration of the organic-walled microfossils, characterized with transmitted light microscopy. The black microfossils correspond to a TAI = ≥5 (Hayes *et al.* 1983), indicating temperatures in the 250–400°C range (Stanevich *et al.* 2005). A CIS value of 0.37 ± 0.04 places the rocks of Little Lawn Harbour slightly above the anchizone-epizone boundary (0.32 Δ2θ), in the anchizone (Warr and Ferreiro-Mahlmann 2015), corresponding to a temperature between 200–300°C, but closer to the 300°C boundary.

Another key indicator for the anchizone is the absence of smectite (Kübler 1967). As burial depth increases, smectite progressively transforms into mixed smectite-illite interlayers (at a temperature of 104°C), and finally, into pure illite (at 137°C) (Aoyagi and Asakawa 1984). Smectite layers tend to hydrate and swell when exposed to ethylene-glycol, causing a shift in the peak positions compared to those of the air-dried sample and these interlayers can be detected by a shift in the oriented clay fraction diffractogram. This shift is absent in our diffractograms, indicating an absence of smectite in the illite structure (for further discussion, see Austermann *et al.* 2021).

The Raman spectra obtained from the specimens of *Bavlinella faveolata* show an arrangement similar to those obtained by Lahfid *et al.* (2010) for rocks of ca. 300°C. Both the D1 and G-bands are narrow, D1 is much narrower than in more poorly organized AOM, and the D4 shoulder is much less pronounced (Bower *et al.* 2013; Álvaro *et al.* 2024), which supports a temperature above 250°C. The G-band peak position is located at 1596.84 ± 1.24 cm^{-1}, which agrees with Beyssac *et al.* (2002) position of the G-band shifts, ranging from 1600 cm^{-1} to ca. 1580 cm^{-1}, as a result of the progressive increase in the metamorphic grade. A peak position <1600 cm^{-1} indicates a metamorphic temperature equal to or higher than 200°C (Rahl *et al.* 2005). The intensity ratio between the two bands, R= 1.17 ± 0.02, is >1, which corresponds to temperatures above 300°C (Lahfid *et al.* 2010) as the intensity of the D-band increases with the metamorphic grade and reaches a maximum at the chlorite facies (lower greenschist), at ca. 300°C, and then decreases, due to the elimination of the crystal lattice defects as perfect graphitic order is approached (Wopenka and Pasteris 1993). This shift is coincident with the split between the G and D2 bands, which are impossible to be separated at lower grades (Lahfid *et al.* 2010).

Although the Peak Resolve software is able to identify all five bands, both D4 and D3 are displaced towards higher wavenumbers (D4 = 1279.13 ± 2.79 cm^{-1}; D3 = 1547.49 ± 3.98 cm^{-1}) than those recorded by Lahfid *et al.* (2010), 1200 cm^{-1} and 1500 cm^{-1}, respectively. This shift is probably controlled by a combination of factors that can induce error in the Raman spectrum (Henry *et al.* 2019), such as: (i) differences in the equipment and experimental setup (e.g., the type of Raman spectrometer used), laser wavelength or sampling parameters; (ii) use of different spectra processing methods, particularly the digital deconvolution of the spectra, as there is no consensus regarding the number of bands or the best-fit profile: e.g., Beyssac *et al.* (2002) used four bands with a Voigt fit, Lahfid *et al.* (2010) used five bands with a Lorentzian fit, and Henry *et al.* (2019) argued against deconvolution and suggested the application of automated spreadsheet procedure for low maturity samples); (iii) differences between sample media: e.g., petrographic thin sections (Beyssac *et al.* 2002), polished kerogen blocks or strew sections; (iv) intra-particle variety and the type of organic matter employed (amorphous organic matter, phytoliths, coals, or identifiable microfossils).

The R2 parameter (Fig. 7a) (R2 = 0.67 ± 0.03) places sample 23AM229 inside the chlorite zone (lower greenschist facies) (Beyssac *et al.* 2002). Two sample points, P6 and P8, have an R2 value >0.7, which indicates a temperature below 330°C. However, these outliers could be the result of intrasample heterogeneity (Henry *et al.* 2019). The RA1 (Fig. 7b) (0.65 ± 0.01) and RA2 (Fig. 7c) (1.65 ± 0.09) ratios and their corresponding temperatures (339.36 ± 16.64°C and 305.81 ± 20.85°C) also fall within the lower greenschists facies. The R2 and RA1 parameters show a degree of overlap in the higher temperature range, although RA2 is significantly lower. The transformed CIS values of the five samples used for illite "crystallinity" place below the anchizone–epizone boundary, delimiting the lower temperature limit (Fig. 7d).

The dispersion values of the area ratios correspond to temperature errors of 15.39°C (R2 = ± 0.03), 5.22°C (RA1 = ± 0.01) and 16.68°C (RA2 = ± 0.09). The σ of R2 is significantly lower than the ± 0.08 reported by Beyssac *et al.* (2002), likely owing to the Henry *et al.* (2019) methodology, which reduces the inherent sampling error and the data dispersion caused by intra-sample heterogeneity. Lahfid *et al.* (2010) also reported a σ of ± 0.01 for RA1, whereas for RA2, the σ falls within their reported range. Beyssac *et al.* (2002) considered the RSCM thermometer to have an expected maximum error of ± 50°C. Again, all three temperature measurements show a σ below that error when converted to degrees (R2 = ± 12.38°C, RA1 = ± 16.54°C, RA2 = ± 20.85°C).

The combined results of XRD analysis and Raman palaeothermometer proxies allow establishment of an upper and lower boundary for the peak metamorphic temperature of sample 23AM229. The standardized CIS and the RA2 parameters delimit a lower boundary close to 300°C, a temperature that marks the anchizone–epizone boundary. The R2 and RA1 parameters, on the other hand, suggest a maximum temperature between 325 and 350°C, within the epizone. In areas with a steep geothermal gradient, such as contact metamorphism zones, the KI and vitrinite reflectance decouple, due to the lower rate of change in clay minerals compared to organic matter (Srodon 1979). This likely

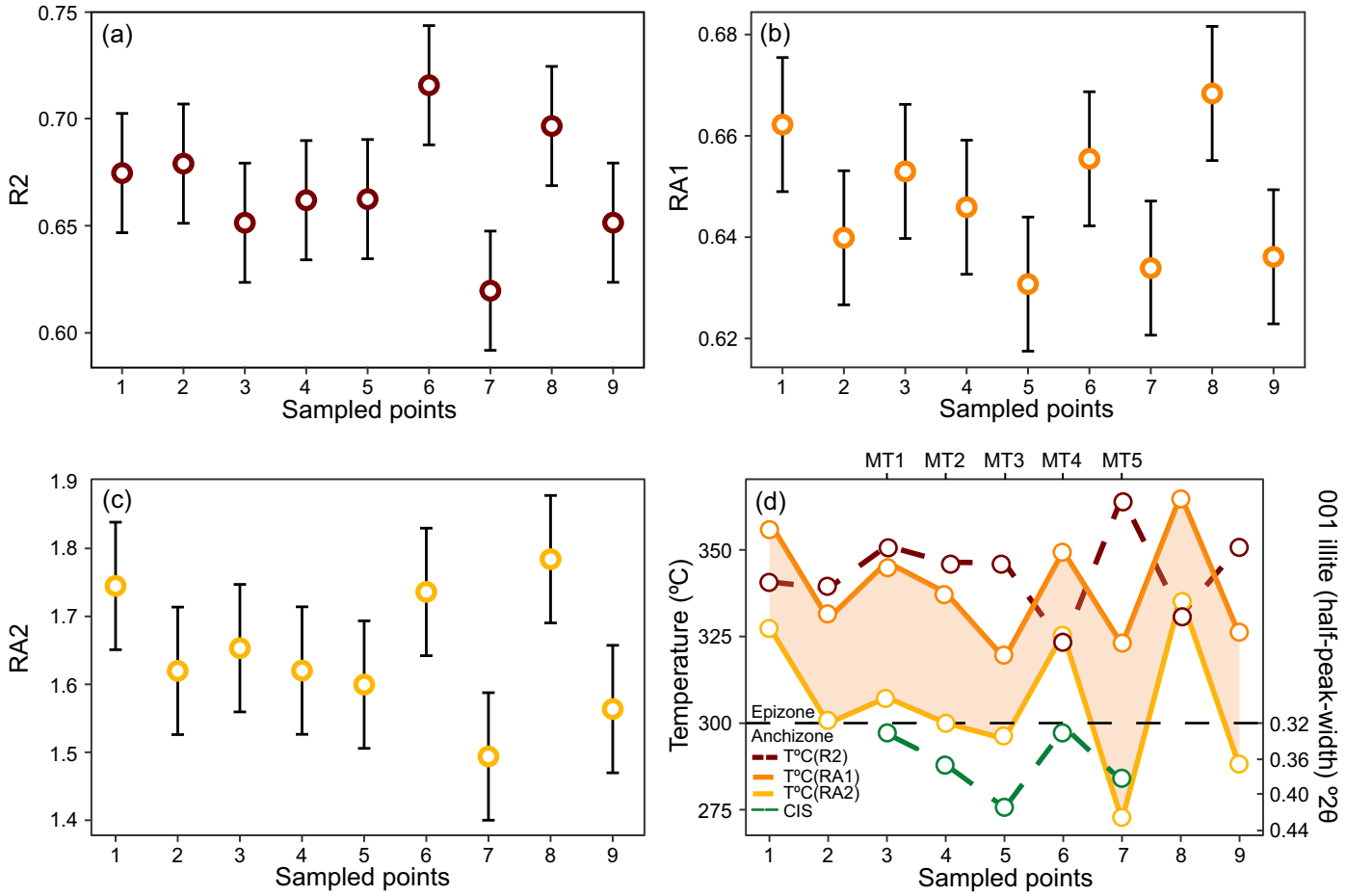

Figure 7. (a) Results of the R2 parameter for the nine sampling points; error bars = 0.03. (b) Results of the RA1 parameter for the nine sampling points; error bars = 0.01. (c) Results of the RA2 parameter for the nine sampling points; error bars = 0.08. (d) Graphic representation of the temperature range obtained for each sampling point by each parameter, alongside the CIS transformed values obtained via X-ray diffraction.

accounts for the slightly lower temperature estimation based on the CIS results relative to those based on RA2.

CONCLUSIONS

The study of Miaolingian black shales from Little Lawn Harbour (Burin Peninsula, Newfoundland) has reported the presence of monospecific associations of the cyanobacterium *Bavlinella faveolata*, and increased the current knowledge regarding the metamorphic evolution of the Burin Peninsula. *Bavlinella faveolata* is a cosmopolitan and stratigraphically long-ranged taxon currently associated with eutrophication processes, despite its problematic taxonomic history. The specimens reported in this work show varying degrees of degradation under thin-section (2D) and FEGSEM (3D). In 3D, their morphology is characterized by spherical forms with a honeycomb cell pattern, with a thin outer vesicle layer that is frequently damaged. The meshwork of amorphous organic matter that is visible in the palynological slides is confirmed to consist of degraded debris of *Bavlinella faveolata* fragments.

The illite crystallinity, the Raman Spectrometry of Carbonaceous Material (RSCM) thermometer, the shape and characteristics of the Raman spectra, and the Thermal Alteration Index of the *Bavlinella faveolata* specimens from sample 23AM229 place it with relative certainty in the 300–350°C range. Two of the Raman thermometers (R2 and RA1) mark the upper boundary of the measurements, with average temperatures of 343.71 ± 12.38°C (R2) and 339.36 ± 16.45°C (RA1), corresponding to beginning of the epizone and the greenschist facies. The RA2 thermometer and the Crystallinity Index Standard (CIS) values indicate a lower boundary, with a slight decoupling between them. RA2 indicates an average temperature of 305.81 ± 20.85°C, with half the datapoints above the deep anchizone–epizone boundary. However, the CIS values place consistently right below or close to the boundary, with an average value of 0.37 ± 0.04. These metamorphic temperatures are consistent with the contact metamorphism in proximity to the St. Lawrence Granite and the strong geothermal gradient generated by contact metamorphism also explains the discrepancies between the RSCM and the CIS results.

ACKNOWLEDGEMENTS

We appreciate the constructive and useful revisions suggested by S. Johnson and an anonymous referee, the laboratory assistance of T. Palacios, the technical support by A.M. Bravo, C. Paradela, I. Theodorou, J.L. Ayala, L. Tormo, and M. Furió (MNCN), and the XRD guidance by F. Nieto and M. Sánchez (Mineralogy and Petrology Department of the University of Granada) and L. Warr (Universität Greifswald), and the support of the Geological Survey of Newfoundland and Labrador. This study was supported by project PID2021-125585NB-I00 funded by the Spanish Ministerio de Ciencia, Innovación y Universidades (MICIU)/Agencia Estatal de Investigación (AEI)/ /10.13039 /501100011033 and the European Social Fund Plus (FSE+).

REFERENCES

Abrámoff, M.D., Magalhaes, P.J., and Ram, S.J. 2004. Image processing with ImageJ. Biophotonics International 11, pp. 36–42.

Álvaro, J.J. 2021. Cambrian syn-rift tectonic pulses at unconformity-bounded carbonates in the Avalon Zone of Newfoundland, Canada. Basin Research, 33, pp. 1520–1545. https://doi.org/10.1111/bre.12525

Álvaro, J.J. and Mills, A. 2024. Carbonate production and reef building under ferruginous seawater conditions in the Cambrian rift branches of the Avalon Zone, Newfoundland. Sedimentology, 71(4), pp. 1–25. https://doi.org/10.1111/sed.13172

Álvaro, J.J., Ortiz, J.E., Neto de Carvalho, C., López-Cilla, I., Sánchez-Palencia, Y., and Torres, T. 2024. Biogenicity of amorphous organic matter and bacteriomorph acritarchs preserved in wrinkle structures from the Ediacaran Cíjara Formation, Spain. The Depositional Record, 10, pp. 51–69. https://doi.org/10.1002/dep2.258

Aoyagi, K. and Asakawa, T. 1984. Paleotemperature analysis by authigenic minerals and its application to petroleum exploration. American Association of Petroleum Geologists Bulletin, 68, pp. 903–913. https://doi.org/10.1306/AD461444-16F7-11D7-8645000102C1865D

Arouri, K.R., Greenwood, P.F., and Walter, M.R. 2000. Biological affinities of Neoproterozoic acritarchs from Australia: microscopic and chemical characterisation. Organic Geochemistry, 31, pp. 75–89. https://doi.org/10.1016/S0146-6380(99)00145-X

Austermann, G., Kling, M., Ifrim, C., Emondt, P.S., Hildebrand, A. 2021. Quantifying the diagenetic impact in the late Ediacaran and early Palaeozoic of the Avalon Peninsula using illite "crystallinity". Canadian Journal of Earth Sciences, 9, pp. 1187–1208. https://doi.org/10.1139/cjes-2020-0207

Bengtson, S. and Fletcher, T. P. 1983. The oldest sequence of skeletal fossils in the Lower Cambrian of southeastern Newfoundland. Canadian Journal of Earth Sciences, 20, pp. 525–536. https://doi.org/10.1139/e83-050

Beny-Bassez, C. and Rouzaud, J.N. 1985. Characterization of carbonaceous materials by correlated electron and optical microscopy and raman microspectroscopy. Scanning Electron Microscopy, 1, pp. 119–132.

Beranek, L.P., Hutter, A.D., Pearcey, S., James, C., Langor, V., Pike, C., Goudie, D., Oldham, L. 2023. New evidence for the Baltican cratonic affinity and Tonian to Ediacaran tectonic evolution of West Avalonia in the Avalon Peninsula, Newfoundland, Canada. Precambrian Research, 390. Article no. 107046, 19 pp. https://doi.org/10.1016/j.precamres.2023.107046

Beyssac, O., Goffé, B., Chopin, C., and Rouzaud, J.N. 2002. Raman spectra of carbonaceous material in metasediments: a new geothermometer. Journal of Metamorphic Geology, 20, pp. 859–871. https://doi.org/10.1046/j.1525-1314.2002.00408.x

Botting, J.P., Muir, L.A., Wang, W., Qie, W., Tan, J., Zhang, L., and Zhang, Y. 2018. Sponge-dominated offshore benthic ecosystems across South China in the aftermath of the end-Ordovician mass extinction. Gondwana Research, 61, pp. 150–171. https://doi.org/10.1016/j.gr.2018.04.014

Bower, D.M., Steele, A., Fries, M.D., and Kater, L. 2013. Micro Raman spectroscopy of carbonaceous material in microfossils and meteorites: improving a method for life detection. Astrobiology, 13, pp. 103–113.https://doi.org/10.1089/ast.2012.0865

Canfield, D.E. and Thamdrup, B.O. 2009. Towards a consistent classification scheme for geochemical environments, or, why we wish the term 'suboxic' would go away. Geobiology, 7, pp. 385–392. https://doi.org/10.1111/j.1472-4669.2009.00214.x

Chiglino, L., Gaucher, C., Sial, A.N., and Ferreira, V.P. 2015. Acritarchs of the Ediacaran Frecheirinha Formation, Ubajara Group, northeastern Brazil. Anais da Academia Brasileira de Ciências, 87, pp. 635–649. https://doi.org/10.1590/0001-3765201520140430

Crimes, T.P. and Anderson, M.M. 1985. Trace fossils from Late Precambrian–Early Cambrian strata of southeastern Newfoundland (Canada): temporal and environmental implications. Journal of Paleontology, pp. 310–343.

Den Uyl, P.A., Harrison, S.B., Godwin, C.M., Rowe, M.D., Strickler, J.R., and Vanderploeg, H.A. 2021. Comparative analysis of Microcystis buoyancy in western Lake Erie and Saginaw Bay of Lake Huron. Harmful Algae, 108. Article no. 102102, 11 pp. https://doi.org/10.1016/j.hal.2021.102102

Douglas, J.L. 1983. Geochemistry of the Cambrian manganese deposits of eastern Newfoundland. Unpublished PhD thesis, Memorial University, St. John's, Newfoundland and Labrador, 328 p.

Downie, C., Lister, T.R., Harris, A.L., and Fettes, D.J. 1971. A palynological investigation of the Dalradian rocks of Scotland. Report of the Institute of Geological Sciences Report, 71, 1–29.

Fletcher, T.P. 2006. Bedrock geology of the Cape St. Mary's Peninsula, southwest Avalon Peninsula, Newfoundland (includes parts of NTS map sheets 1M/1, 1N/4, 1L/16 and

1K/13). Government of Newfoundland and Labrador, Department of Natural Resources, Geological Survey, Report 06-2, pp. 1–137.

Foster, C.B., Cernovskis, A., and O'Brien, G.W. 1985. Organic-walled microfossils from the Early Cambrian of South Australia. Alcheringa: an Australasian Journal of Palaeontology, 9, pp. 259–268. https://doi.org/10.1080/03115518508618972

Frei, R., Gaucher, C., Stolper, D., and Canfield, D.E. 2013. Fluctuations in late Neoproterozoic atmospheric oxidation - Cr isotope chemostratigraphy and iron speciation of the late Ediacaran lower Arroyo del Soldado Group (Uruguay). Gondwana Research, 23, pp. 797–811. https://doi.org/10.1016/j.gr.2012.06.004

Gaucher, C. 2000. Sedimentology, palaeontology and stratigraphy of the Arroyo del Soldado Group (Vendian to Cambrian, Uruguay). Beringeria, 608, 62 pp.

Gaucher, C. and Germs, G. J. B. 2006. Recent advances in South African Neoproterozoic–Early Palaeozoic biostratigraphy: correlation of the Cango Caves and Gamtoos groups and acritarchs of the Sardinia Bay Formation, Saldania Belt. South African Journal of Geology, 109, pp. 193–214. https://doi.org/10.2113/gssajg.109.1-2.193

Gaucher, C. and Sprechmann, P. 1999. Upper Vendian skeletal fauna of the Arroyo del Soldado Group, Uruguay. Beringeria, 23, pp. 55–91.

Gaucher, C., Boggiani, P., Sprechmann, P., Sial, A., and Fairchild, T. 2003. Integrated correlation of the Vendian to Cambrian Arroyo del Soldado and Corumbá groups (Uruguay and Brazil): palaeogeographic, palaeoclimatic and palaeobiologic implications. Precambrian Research, 120, pp. 241–278. https://doi.org/10.1016/S0301-9268(02)00140-7

Gaucher, C., Chiglino, L., and Peçoits, E. 2004. Southernmost xxposures of the Arroyo del Soldado Group (Vendian to Cambrian, Uruguay): palaeogeographic implications for the amalgamation of W-Gondwana. Gondwana Research, 7, pp. 701–714. https://doi.org/10.1016/S1342-937X(05)71057-1

Gaucher, C., Frimmel, H.E., and Germs, G. J. B. 2005. Organic-walled microfossils and biostratigraphy of the upper Port Nolloth Group (Namibia): implications for latest Neoproterozoic glaciations. Geological Magazine, 142, pp. 539–559. https://doi.org/10.1017/S0016756805001123

Gaucher, C., Blanco, G., Chiglino, L., Poiré, D., and Germs, G.J. 2008. Acritarchs of Las Ventanas Formation (Ediacaran, Uruguay): implications for the timing of coeval rifting and glacial events in western Gondwana. Gondwana Research, 13, pp. 488–501. https://doi.org/10.1016/j.gr.2007.05.008

German, T.N., Mikhajlova, N.S., and Yankauskas, T.V. 1989. Sistematicheskoe opisanie mikrofossilij [Systematic description of microfossils]. *In* Mikrofossilii Dokembriya SSSR [Precambrian Microfossils of the USSR]. *Edited by* T.V. Yankauskas. Leningrad, Nauka, pp. 34–151.

Hagenfeldt, S.E., Palmlöv, E., Amantov, A., Hagström, J., Ghalayini, R., and Liljedahl, T. 2023. The development of dark shales from the middle and late Cambrian to early Ordovician on the East European Platform-with focus on Gotland. GFF, 145, pp. 30–49. https://doi.org/10.1080/11035897.2023.2251154

Hayes, J.M., Kaplan, I.R., and Wedeking, W. 1983. Precambrian organic geochemistry, preservation of the record. *In* Earth's Earliest Biosphere. *Edited by* J.W. Schopf. Princeton University Press, pp. 93–134

Henry, D.G., Jarvis, I., Gillmore, G., and Stephenson, M. 2019. Raman spectroscopy as a tool to determine the thermal maturity of organic matter: application to sedimentary, metamorphic and structural geology. Earth-Science Reviews, 198. Article no. 102936, 19 pp. https://doi.org/10.1016/j.earscirev.2019.102936

Hutchinson, R.D. 1962. Cambrian stratigraphy and trilobite faunas of southeastern Newfoundland. Geological Survey of Canada, Department of Mines and Technical Surveys, 43 pp. https://doi.org/10.4095/123902

Johnson, S., White, C.E., Palacios, T., Jensen, S., and Barr, S.M. 2024. Middle Cambrian (Miaolingian) acritarchs from the Flagg Cove Formation, Grand Manan Island, New Brunswick, Canada: stratigraphic implications and possible correlations. Atlantic Geoscience, 60, pp. 63–75. https://doi.org/10.4138/atlgeo.2024.004.

Kelly, L. J., Fauria, K.E., Mittal, T., El Kassar, J., Bennartz, R., Nicholson, D., Subramaniam, A., and Gupta, A.K. 2023. Ash deposition triggers phytoplankton blooms at Nishinoshima volcano, Japan. Geochemistry, Geophysics, Geosystems, 24, pp. 1–22. https://doi.org/10.1029/2023GC010914

Kennedy, M.J., Pevear, D.R., and Hill, R.J. 2002. Mineral surface control of organic carbon in black shale. Science, 295, pp. 657–660. https://doi.org/10.1126/science.1066611

Kerr, A., Dunning, G.R., and Tucker, R.D. 1993. The youngest Paleozoic plutonism of the Newfoundland Appalachians: U-Pb ages from the St. Lawrence and François granites. Canadian Journal of Earth Sciences, 30, pp. 2328–2333. https://doi.org/10.1139/e93-202

Kisch, H.J. 1991. Illite crystallinity: recommendations on sample preparation, X-ray diffraction settings, and interlaboratory samples. Journal of Metamorphic Geology, 9, pp. 665–670. https://doi.org/10.1111/j.1525-1314.1991.tb00556.x

Kübler, B. 1967. La cristallinité de l'illite et les zones tout á fait supérieures du métamorphisme. Etages Tectoniques, Colloque de Neuchâtel 1966. Univ. Neuchâtel à la Baconnière, Suisse, pp. 105–121.

Kützing, F.T. 1833. Synopsis diatomearum oder Versuch einer systematischen Zusammenstellung der Diatomeen. Linnaea, 8, pp. 529–620. https://doi.org/10.5962/bhl.title.65634

Lahfid, A., Beyssac, O., Deville, E., Negro, F., Chopin, C., and Goffé, B. 2010. Evolution of the Raman spectrum of carbonaceous material in low-grade metasediments of the Glarus Alps (Switzerland). Terra Nova, 22, pp. 354–360. https://doi.org/10.1111/j.1365-3121.2010.00956.x

Landing, E. and Westrop, S.R. 1998. Avalon 1997-The Cam-

brian Standard. The international field conference of the Cambrian Chronostratigraphy Working Group. IGCP Project 366 (Ecological aspects of the Cambrian radiation). New York State Museum Bulletin 492, 92 p.

Landis, C.A. 1971. Graphitization of dispersed carbonaceous material in metamorphic rocks. Contributions to Mineralogy and Petrology, 30, pp. 34–45. https://doi.org/10.1007/BF00373366

Large, R.R., Halpin, J.A., Lounejeva, E., Danyushevsky, L.V., Maslennikov, V.V., Gregory, D., Sack, P., Haines, P.W., Long, J.A., Makoundi, C., Stepanov, A.S. 2015. Cycles of nutrient trace elements in the Phanerozoic ocean. Gondwana Research, 28, 1282–1293. https://doi.org/10.1016/j.gr.2015.06.004

Le Hérissé, A., Vecoli, M., Guidat, C., Not, F., Vecoli, M., Breuer, P., Wellman, C., and Steemans, P. 2017. Middle Ordovician acritarchs and problematic organic-walled microfossils from the Saq-Hanadir transitional beds in the QSIM-801 well, Saudi Arabia. Revue de Micropaléontologie, 60, pp. 289–318. https://doi.org/10.1016/j.revmic.2017.08.001

Longman, J., Mills, B.J., Manners, H.R., Gernon, T.M., and Palmer, M.R. 2021. Late Ordovician climate change and extinctions driven by elevated volcanic nutrient supply. Nature Geoscience, 14, pp. 924–929. https://doi.org/10.1038/s41561-021-00855-5

Love, L.G. 1958. Micro-organisms and the presence of syngenetic pyrite. Quarterly Journal of the Geological Society of London, 113, pp. 429–440. https://doi.org/10.1144/GSL.JGS.1957.113.01-04.18

MacLean, L.C.W., Tyliszczak, T., Gilbert, P.U.P.A., Zhou, D., Pray, T.J., Onstott, T.C., and Southam, G. 2008. A high-resolution chemical and structural study of framboidal pyrite formed within a low-temperature bacterial biofilm. Geobiology, 6, pp. 471–480. https://doi.org/10.1111/j.1472-4669.2008.00174.x

Magyarosi, Z., Sparkes, B.A., Conliffe, J., and Dunning, G.R. 2019. The AGS fluorite deposit, St. Lawrence: paragenetic sequence, fluid inclusion analysis, structural control, host rock geochronology and implications for ore genesis. *In* Current Research. Government of Newfoundland and Labrador, Department of Natural Resources, Geological Survey, Report 19-1, pp. 59–83.

Mansuy, C. and Vidal, G. 1983. Late Proterozoic Brioverian microfossils from France: taxonomic affinity and implications of plankton productivity. Nature, 302, pp. 606–607. https://doi.org/10.1038/302606a0

Marshall, C.P., Javaux, E.J., Knoll, A.H., and Walter, M. . 2005. Combined micro-Fourier transform infrared (FTIR) spectroscopy and micro-Raman spectroscopy of Proterozoic acritarchs: a new approach to Palaeobiology. Precambrian Research, 138, pp. 208–224. https://doi.org/10.1016/j.precamres.2005.05.006

Martin, R.E. 1996. Secular increase in nutrient levels through the Phanerozoic: Implications for productivity, biomass, and diversity of the marine biosphere. Palaios, 11, pp. 209–219. https://doi.org/10.2307/3515230

Martin, F. and Dean, W.T. 1981. Middle and Upper Cambrian and Lower Ordovician acritarchs from Random Island, eastern Newfoundland. Canada Geological Survey Bulletin, 343, pp.1–43. https://doi.org/10.4095/124915

McCartney, W.D. 1967. Whitbourne map-area, Newfoundland. Geological Survey of Canada, Memoir, 341, pp. 1–135. https://doi.org/10.4095/123895

Menges, F. 2022. Spectragryph - optical spectroscopy software, Version 1.1.16.1, 2022, http://www.effemm2.de/spectragryph/

Mills, A. and Álvaro, J.J. 2023. Lithogeochemical features of Cambrian basalts from western Avalon Peninsula, Avalon Terrane, Newfoundland: alkaline magmatism along an inherited fault zone. Current Research, 23, pp. 1–24.

Mills, A. and Jones, V. 2024. New structural observations on the southern Burin Peninsula, Avalon zone, Newfoundland. Newfoundland and Labrador Department of Industry, Energy and Technology Geological Survey, 24-1, pp. 181–204. http://doi.org/10.13140/RG.2.2.34217.61282

Moorman, M. 1974. Microbiota of the Late Proterozoic Hector Formation, southwestern Alberta, Canada. Journal of Paleontology, 48, pp. 524–539.

Muir, M.D. 1977. Late Precambrian microfossils. Geological Magazine, 114, pp. 395–397. https://doi.org/10.1017/S0016756800036712

Nagy, R.M., Porter, S.M., Dehler, C.M., and Shen, Y. 2009. Biotic turnover driven by eutrophication before the Sturtian low-latitude glaciation. Nature Geoscience, 2, pp. 415–418. https://doi.org/10.1038/ngeo525

Nance, R.D., Murphy, J.B., and Keppie, J.D. 2002. A Cordilleran model for the evolution of Avalonia. Tectonophysics, 352, pp. 11–31. https://doi.org/10.1016/S0040-1951(02)00187-7

Nance, R.D., Murphy, J.B., Strachan, R.A., Keppie, J.D., Gutiérrez-Alonso, G., Fernández-Suárez, J., Quesada, C., Linnemann, U., D'lemos, R., and Pisarevsky, S.A. 2008. Neoproterozoic-early Palaeozoic tectonostratigraphy and palaeogeography of the peri-Gondwanan terranes: Amazonian v. West African connections. Geological Society, London, Special Publications, 297, pp. 345–383. https://doi.org/10.1144/SP297.17

Narbonne, G.M., Myrow, P.M., Landing, E., and Anderson, M.M. 1987. A candidate stratotype for the Precambrian-Cambrian boundary, Fortune head, Burin Peninsula, southeastern Newfoundland. Canadian Journal of Earth Sciences, 24, pp. 1277–1293. https://doi.org/10.1139/e87-124

Nielsen, A.T. and Schovsbo, N.H. 2007 Cambrian to basal Ordovician lithostratigraphy in southern Scandinavia. Bulletin of the Geological Society of Denmark, 53, pp. 47–92. https://doi.org/10.37570/bgsd-2006-53-04

O'Brien, S.J., Strong, P.G., and Evans, J.L. 1977. The geology of the Grand Bank (1M/4) and Lamaline (1L/13) map areas, Burin Peninsula, Newfoundland. Government of Newfoundland and Labrador, Department of Mines and Energy, Mineral Development Division, Report 77-7, pp. 1–20.

O'Brien, S.J., Strong, D.G., and King, A.F. 1990. The Avalon zone type area: southeastern Newfoundland Appalachians. *In* Avalonian and Cadomian geology of the North Atlantic. *Edited by* R.A. Strachan andG.K. Taylor. Glasgow, Blackies and Son, pp. 166–194.

O'Brien, S.J., O'Brien, B.H., Dunning, G.R., and Tucker, R.D. 1996. Late Neoproterozoic Avalonian and related peri-Gondwanan rocks of the Newfoundland Appalachians. *In* Avalonian and Related Peri-Gondwanan Terranes of the Circum-North Atlantic. *Edited by* R.D. Nance and M.D. Thompson. Geological Society of America Memoir, pp. 9–28. https://doi.org/10.1130/0-8137-2304-3.9

Palacios, T. 1983. Primeros microfósiles de pared orgánica extraídos en el Olistostroma del Membrillar (Proterozoico Superior del Centro de España). Revista Española de Micropaleontología, 15, pp. 511–517.

Palacios, T., Jensen, S., White, C.E., and Barr, S.M. 2011. Cambrian acritarchs from the Bourinot belt, Cape Breton Island, Nova Scotia: age and stratigraphic implications. Canadian Journal of Earth Sciences, 49, pp. 1–19. https://doi.org/10.1139/e11-010

Palacios, T., Högström, A.E.S., Jensen, S., Ebbestad, J.O.R., Agić, H., Høyberget, M., Meinhold, G., and Taylor, W. L. 2022. Organic-walled microfossils from the Kistedalen Formation, Norway: acritarch chronostratigraphy of the Baltic Miaolingian and evolutionary trends of placoid acritarchs. Papers in Palaeontology, 8, pp. 41–57. https://doi.org/10.1002/spp2.1457

Papezik, V.S. 1974. Prehnite-pumpellyite facies metamorphism of late Precambrian rocks of the Avalon Peninsula, Newfoundland. The Canadian Mineralogist, 12, pp. 463–468.

Pasteris, J.D. and Wopenka, B. 2003. Necessary, but not sufficient: Raman identification of disordered carbon as a signature of ancient .ife. Astrobiology, 3, pp. 727–738. https://doi.org/10.1089/153110703322736051

Pflug, H. D. and Reitz, E. 1992. Palynostratigraphy in Phanerozoic and Precambrian metamorphic rocks. *In* Early organic evolution: implications for mineral and energy resources. *Edited by* M. Schidlowski, S. Golubic, M.M. Kimberley, D.M. McKirdy, and P.A. Trudinger. Berlin, Heidelberg, Springer, pp. 509–518. https://doi.org/10.1007/978-3-642-76884-2_41

Plotnick, R.E. and Wagner, P.J. 2006. Round up the usual suspects: common genera in the fossil record and the nature of wastebasket taxa. Paleobiology, 32, pp. 126–146. https://doi.org/10.1666/04056.1

Prasad, B., Asher, R., and Borgohai, B. 2010. Late Neoproterozoic (Ediacaran) –Early Paleozoic (Cambrian) acritarchs from the Marwar Supergroup, Bikaner-Nagaur Basin, Rajasthan. Journal of the Geological Society of India, 75, pp. 415–431. https://doi.org/10.1007/s12594-010-0038-4

Rahl, J.M., Anderson, K.M., Brandon, M.T., and Fassoulas, C. 2005. Raman spectroscopic carbonaceous material thermometry of low-grade metamorphic rocks: Calibration and application to tectonic exhumation in Crete, Greece. Earth and Planetary Science Letters, 240, pp. 339-354. https://doi.org/10.1016/j.epsl.2005.09.055

Reitz, E. 1991. Acritarchen des Unter-Tremadoc aus dem westlichen Frankenwald, NE-Bayern (Acritarchs of early Tremadoc sediments in the western Frankenwald area, NE Bavaria). Neues Jahrbuch für Geologie und Paläontologie, Monatshefte, 2, pp. 97–104. https://doi.org/10.1127/njgpm/1991/1991/97

Rees, A.J., Thomas, A.T., Lewis, H.E., Hughes, W., and Turner, P. 2014. The Cambrian of SW Wales: towards a unified Avalonian stratigraphy. Geological Society of London, Memoir 12, 640 pp. https://doi.org/10.1144/M42.0

Rushton, A.W.A. 2011. Chronostratigraphical subdivisions of the Cambrian Period. *In*: A revised correlation of the Cambrian rocks in the British Isles. *Edited by* A.W.A. Rushton, P.M. Brück, S.G. Molyneux, M. Williams, and N.H. Woodcock. Geological Society, Special Reports, 25, pp. 3–5. https://doi.org/10.1144/SR25.2

Sageman, B.B., Murphy, A.E., Werne, J.P., Ver Straeten, C.A., Hollander, D.J., and Lyons, T.W. 2003. A tale of shales: the relative roles of production, decomposition, and dilution in the accumulation of organic-rich strata, Middle-Upper Devonian, Appalachian basin. Chemical Geology, 195, pp. 229–273. https://doi.org/10.1016/S0009-2541(02)00397-2

Satkoski, A.M., Barr, S.M., and Samsom, S.D. 2010. Provenance of Late Neoproterozoic and Cambrian sediments in Avalonia: constraints from detrital zircon ages and Sm–Nd isotopic compositions in southern New Brunswick, Canada. Journal of Geology, 118, pp. 187–200. https://doi.org/10.1086/649818

Savitzky, A. and Golay, M.J.E. 1964. Smoothing and differentiation of data by simplified least squares procedures. Analytical Chemistry, 36, pp. 1627–1639. https://doi.org/10.1021/ac60214a047

Schils, T. 2012. Episodic eruptions of volcanic ash trigger a reversible cascade of nuisance species outbreaks in pristine coral habitats. PLoS ONE, 7, pp. 1–7. https://doi.org/10.1371/journal.pone.0046639

Schopf, J.W. 1992. Atlas of representative Proterozoic microfossils. *In* The Proterozoic biosphere-a multidisciplinary study. *Edited by* J.W. Schopf and C. Klein. Cambridge University Press, Cambridge, pp. 1054–1117. https://doi.org/10.1017/CBO9780511601064

Shepeleva, E.D. 1962. Rastilel'nyye(?) ostatki neizvestnoy sistematicheskoy prinadlezhnosti iz otlozheniy bavlinskoy serii Volgo-Ural'skoy neftenosnoy provintsii. [(Plant? fossils of unknown taxonomic position from deposits of the Bavlinskaya Series in the Volga-Urals oil province)] Dokl. Akad. Nauk. SSR, 142, pp. 456–457.

Shkrebta, G.P., Antipov, V.I., and Lashmanova, R.M. 1973. New data on the age of ancient deposits in the Dnieper Donetzs Basin. Byulleten Moskovskogo Obshchestva Ispytatelei Prirody, Otdel Geologicheskii (Bulletin of the Moscow Nature Researchers' Society, Geological Department), 48, pp. 59–65 [in Russian].

Sparkes, G. and Dunning, G. 2014. Late Neoproterozoic epithermal alteration and mineralization in the western Avalon zone: a summary of mineralogical investigations and new U–Pb geochronological results. Current Research Newfoundland and Labrador Department of Natural Resources, Geological Survey, Report, 14-1, pp. 99–128.

Srodon, J. 1979. Correlation between coal and clay diagenesis in the Carboniferous of the Upper Silesian Coal Basin. Developments in sedimentology, 27, pp. 251–260. https://doi.org/10.1016/S0070-4571(08)70721-0

Stanevich, A.M., Nemerov, V.K., Sovetov Yu, K., Chatta, E.N., Mazukabzov, A.M., Perelyaev, V.I. and Kornilova, T.A. 2005. Precambrian microfossil-characterized biotopes from the southern margin of the Siberian craton. Russian Journal of Earth Sciences, 7, pp. 1–28. https://doi.org/10.2205/2005ES000183

Stanier, R.Y., Sistrom, W.R., Hansen, T.A. *et al.* 1978. Proposal to place the nomenclature of the cyanobacteria (blue-green algae) under the rules of the International Code of Nomenclature of Bacteria. International Journal of Systematic and Evolutionary Microbiology, 28, pp. 335–336. https://doi.org/10.1099/00207713-28-2-335

Strong, D.F., O'Brien, S.J., Strong, P.G., Taylor, S.W., and Wilton, D.H. 1976. Geology of the St. Lawrence and Marystown map sheets (1L/14, 1M/3), Newfoundland. Government of Newfoundland and Labrador, Department of Mines and Energy, Mineral Development Division, Open File Report, 895, pp. 1–44.

Strong, D.F., O'Brien, S.J., Taylor, S.W., Strong, P.G., and Wilton, D.H. 1978. Geology of Marystown (1M/3) and St. Lawrence (1L/14) map areas, Newfoundland. Government of Newfoundland and Labrador, Department of Mines and Energy, Mineral Development Division, Report, 77-8, pp. 1–81.

Tuinstra, F. and Koenig, J.L. 1970. Raman spectrum of graphite. The Journal of Chemical Physics, 53, pp. 1126–1130. https://doi.org/10.1063/1.1674108

Van Alstine, R.E. 1948. Geology and mineral deposits of the St. Lawrence area, Burin Peninsula, Newfoundland. Geological Survey of Newfoundland Bulletin, 43, pp. 1–64.

van Staal, C.R., Barr, S.M., McCausland, P.M., Thompson, M.D., and White, C.E. 2020. Tonian–Ediacaran tectonomagmatic evolution of West Avalonia and its Ediacaran–Early Cambrian interactions with Ganderia: an example of complex terrane transfer due to arc-arc collision? *In* Pannotia to Pangaea: Neoproterozoic and Paleozoic orogenic cycles in the circum-Atlantic region. *Edited by* J.B. Murphy, R.A. Strachan, and C. Quesada. Geological Society, London, Special Publications, 503, pp. 143–167. https://doi.org/10.1144/SP503-2020-23

Vavrdová, M. 2008. Proterozoic acritarchs from the Precambrian–Cambrian transition in southern Moravia. Bulletin of Geosciences, 83, pp. 85–92. https://doi.org/10.3140/bull.geosci.2008.01.085

Vidal, G. 1976. Late Precambrian microfossils from the Visingsö Beds in southern Sweden. Fossils and Strata, 9, pp. 1–57. https://doi.org/10.18261/8200094189-1976-01

Vidal, G. 1988. A palynological preparation method. Palynology, 12, pp. 215–220. https://doi.org/10.1080/01916122.1988.9989345

Vidal, G. and Nystuen, J.P. 1990. Micropaleontology, depositional environment and biostratigraphy of the upper Proterozoic Hedmark Group, southern Norway. American Journal of Science, 290-A, pp. 261–294.

Warr, L.N. 2018. A new collection of clay mineral 'Crystallinity'Index Standards and revised guidelines for the calibration of Kübler and Árkai indices. Clay Minerals, 53, pp. 339–350. https://doi.org/10.1180/clm.2018.42

Warr, L.N. and Rice, A.H.N. 1994. Interlaboratory standardization and calibration of day mineral crystallinity and crystallite size data. Journal of metamorphic Geology, 12, pp. 141–152. https://doi.org/10.1111/j.1525-1314.1994.tb00010.x

Warr, L.N. and Ferreiro-Mählmann, R.F. 2015. Recommendations for Kübler index standardization. Clay Minerals, 50, pp. 283–286. https://doi.org/10.1180/claymin.2015.050.3.02

Wopenka, B. and Pasteris, J.D. 1993. Structural characterization of kerogens to granulite-facies graphite: applicability of Raman microprobe spectroscopy. American mineralogist, 78, pp. 533–557.

Wu, X., Luo, H., Zhang, J., Chen, Q., Fang, X., Wang, W., Li, W., Shi, Z., and Zhang, Y. 2023. Volcanism-driven marine eutrophication in the end-Ordovician: evidence from radiolarians and trace elements of black shale in South China. Journal of Asian Earth Sciences, 253, pp. 1–12. https://doi.org/10.1016/j.jseaes.2023.105687

Yin, L. and Yuan, X. 2007. Radiation of Meso-Neoproterozoic and early Cambrian protists inferred from the microfossil record of China. Palaeogeography, Palaeoclimatology, Palaeoecology, 254, pp. 350–361. https://doi.org/10.1016/j.palaeo.2007.03.028

Yin, L.M., Singh, B.P., Bhargava, O.N., Zhao, Y.L., Negi, R.S., Meng, F.W., and Sharma, C.A. 2018. Palynomorphs from the Cambrian Series 3, Parahio valley (Spiti), Northwest Himalaya. Palaeoworld, 27, pp. 30–41. https://doi.org/10.1016/j.palwor.2017.05.004

Zhang, J., Li, W., Fang, X., Wu, X., Li, C., and Zhang, Y. 2024. Marine eutrophication within the Tarim Platform in sync with Middle to Late Ordovician climatic cooling. Journal of the Geological Society, 181, pp.1–8. https://doi.org/10.1144/jgs2023-078

Editorial responsibility: Chris E. White